







ORIGINAL RESEARCH

Transformerless partial power converter topology for electric vehicle fast charge

Daniel Pesantez¹  | Hugues Renaudineau¹  | Sebastian Rivera^{2,3}  |
Alejandro Peralta¹  | Abraham Marquez Alcaide⁴  | Samir Kouro^{1,4} 

¹Department of Electronic Engineering, Universidad Técnica Federico Santa María, Valparaíso, Chile

²Department of Electrical Sustainable Energy – DCE&S Group, Delft University of Technology, South Holland, Netherlands

³Department of Electrical Engineering, Universidad Católica de la Santísima Concepción, Concepción, Chile

⁴Department of Electronic Engineering, Universidad de Sevilla, Sevilla, Spain

Correspondence

Daniel Pesantez, Department of Electronic Engineering, Universidad Técnica Federico Santa María, Valparaíso, Chile.
Email: alvaro.pesantez@sansano.usm.cl

Funding information

SERC, Grant/Award Number: ANID/FONDAP/1522A0006; Fondo Nacional de Desarrollo Científico y Tecnológico, Grant/Award Number: Fondecyt/1221741; AC3E, Grant/Award Number: AC3E (ANID/BASAL/FB0008); Universidad Técnica Federico Santa María, Grant/Award Number: Dirección de Postgrado y Programas Universidad T; Agencia Nacional de Investigación y Desarrollo, Grant/Award Numbers: Doctorado Nacional/2022/21221405, FONDEQUIP/EQM180215

Abstract

Increasing the power rating of electric vehicles (EV) fast charging stations to reduce charging times is considered critical to accelerate the adoption of electric vehicles. Besides increasing the power, other drivers pushing the development of EV fast chargers include the improvement of efficiency and reliability. Partial power converters (PPC) have emerged as an interesting option for some of the power converter stages in fast charging stations due to their potential to increase efficiency and power rating. However, some PPCs operate as switched autotransformers by using high frequency (HF) isolation transformers but without providing galvanic isolation. This is a drawback due to cost, size and losses introduced by the transformer. This paper presents a transformerless DC–DC Type I step-up PPC for a DC–DC regulation converter for EV fast charging stations. The proposed converter replaces the transformer commonly used in Type I PPC by an impedance network, resulting in a more efficient, cheaper, and less complex converter option. This concept is verified through simulations and experimentally validated with a laboratory prototype.

1 | INTRODUCTION

Electric vehicle adoption has been increasing over 40% annually over the last five years, reaching a share of 14% of global sales in 2022, which led to 2.1% of the worldwide car stock in 2022 [1]. This transition is accelerating mainly due to environmental concerns, reduction in EV costs, governmental incentives, and improvements in battery technology (range and lifespan), which have positively impacted users' confidence in this technology [2–4]. Conversely, the uptake of electric vehicles has been impeded by the presence of multiple, ever-changing charging standards and a lack of fast chargers around the world.

The advancements in ion-lithium (Li-ion) battery technology have positioned it as the preferred choice among EV manufacturers, making EVs more cost-effective and practical [3–7]. In

particular, the industry has significantly improved EV batteries' nominal voltage, shifting from typical 400 V architectures to 800 V. Higher voltage batteries enable an increase in the peak efficiency for the powertrain and more importantly in the battery charging process. The development of EV batteries has gone hand in hand with the progress in battery chargers [3, 4]. Nowadays, commercially available fast charging stations reach charging rates up to 600 kW per cabinet, and it is estimated that this charging power will continue to grow as the market matures [8].

Currently, the mainstream solution for EV fast chargers is a two-stage power conversion system (AC–DC followed by DC–DC) employing fully rated power converters [3, 9–11]. For traditional 400 V battery architectures, a typical grid connection to 400 Vac would require a buck DC–DC stage to regulate the

This is an open access article under the terms of the [Creative Commons Attribution-NonCommercial-NoDerivs](https://creativecommons.org/licenses/by-nc-nd/4.0/) License, which permits use and distribution in any medium, provided the original work is properly cited, the use is non-commercial and no modifications or adaptations are made.

© 2023 The Authors. *IET Power Electronics* published by John Wiley & Sons Ltd on behalf of The Institution of Engineering and Technology.

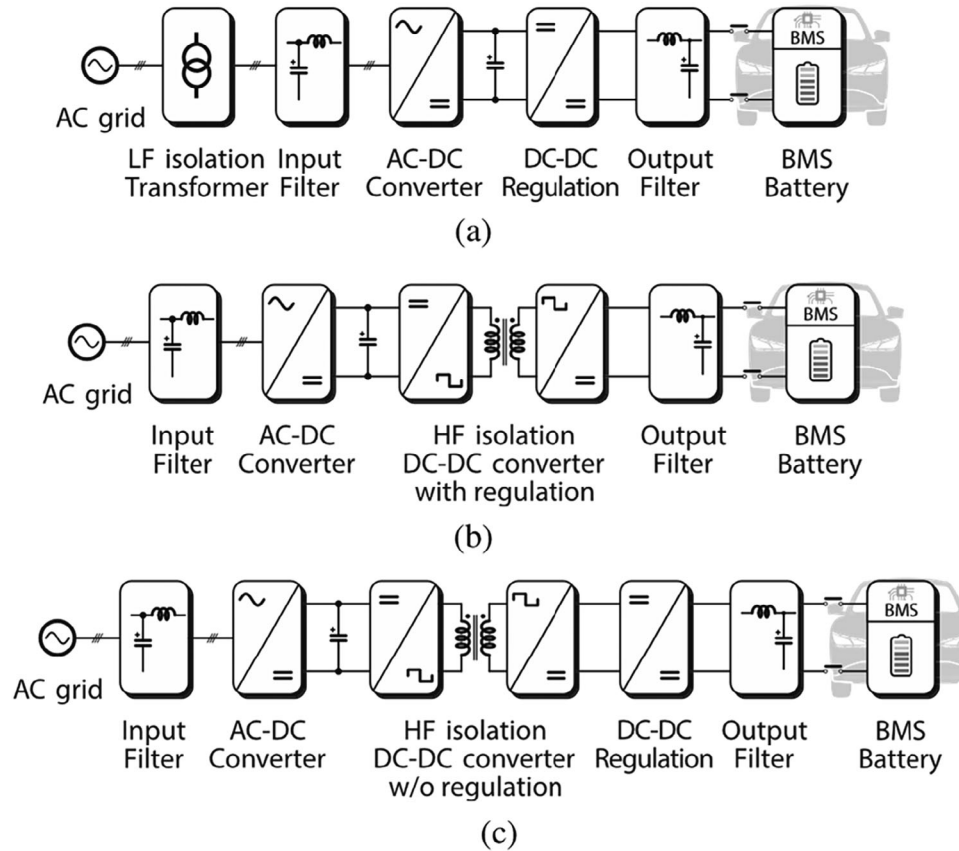


FIGURE 1 General Structure of an EV battery charger. (a) With low-frequency isolation. (b) With regulated high-frequency isolation. (c) With unregulated high-frequency isolation and post-regulation.

battery charging process. In contrast newer EVs employing 800 V architecture battery systems, in most cases the DC-link will be lower than the battery voltage, requiring the DC-DC converter to step-up the voltage so the charging process can be carried out correctly. Several topologies of boost converters for charging stations can be found in the literature [12–14].

On the other hand, existing regulation requires galvanic isolation between the battery and the grid, which can be implemented either at low frequency (LF) at the grid side or at high frequency (HF) as a part of the DC-DC stage [3–5], as shown in Figure 1. For EV chargers feeding from a common DC bus, galvanic isolation is still required between EVs, for which the HF transformer in the DC-DC stages shown in Figure 1b,c are still necessary [15]. Typical topologies include regulated DC-DC converters with HF isolation such as the dual active bridge for configurations like in Figure 1b, and unregulated soft-switched resonant converters followed by a post-regulation DC-DC stage for the case shown in Figure 1c. In all these solutions the DC-DC stage connects the DC bus, at the output of the AC-DC converter, with the battery and is responsible of controlling the current fed to the battery according to the charging profile.

The advantage of using a HF isolation stage without regulation and using a post-regulation DC-DC converter as in Figure 1c, is that higher efficiencies can be achieved in the isolation transformer due to fixed input-output voltage operation.

When the input voltage of a transformer varies, the magnetic flux in its core changes accordingly, resulting in a variation in the output voltage. This voltage fluctuation leads to losses in the transformer's core due to hysteresis and the induced eddy currents [16]. For example, LLC resonant converters are widely used in various applications and especially for battery charging, due to their straightforward design and high efficiency achieved through zero-voltage switching (ZVS) and zero-current switching (ZCS) operation. However, this efficiency drops significantly when the input and output voltages vary, causing the converter to operate far from its resonant frequency. In order to ensure maximum efficiency in the operation of the converter, the input and output voltages of the converter can be maintained at its optimal operation point, and an additional DC-DC without isolation regulation stage can be added to allow output voltage regulation. In [17], a comparison of the overall efficiency of a two-stage full-bridge LLC converter and an HF isolation converter without regulation that utilizes a post-regulation DC-DC converter stage is presented. This motivates the search for more efficient topologies for the regulating DC-DC converter. An interesting alternative are partial power converters (PPC), a family of converters that can reduce losses, size and weight, and even the cost of the converter [18–21]. PPCs are characterized by using topologies that process a fraction of the total power, thus allowing a reduction in power losses and converter size without sacrificing functionality. Several PPCs, previously

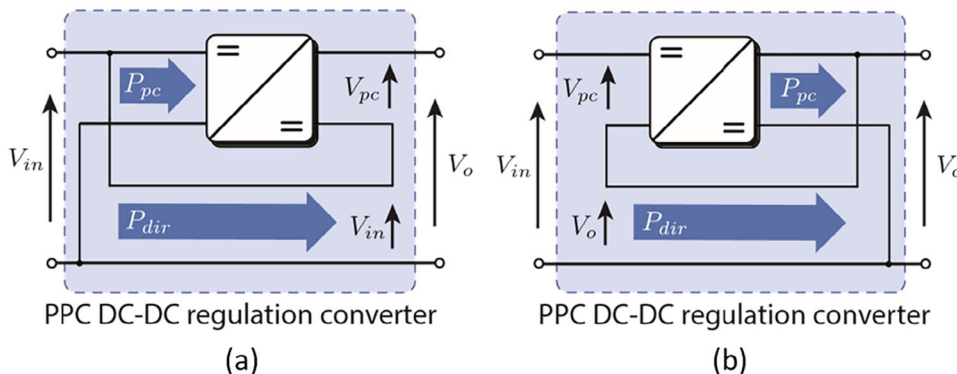


FIGURE 2 General structure of a PPC DC–DC regulation converter. (a) Type I PPC. (b) Type II PPC.

proposed to operate as the DC–DC stage of charging stations, are detailed in [20–24].

As it can be observed in Figure 2, two interconnections’ possibilities for PPC exist namely, input-parallel output-series (IPOS) or input-series output-parallel (ISOP), also known as Type I and Type II PPC respectively. In these configurations, P_{pc} represents the power handled by the converter, P_{dir} represents the power that goes directly to the battery, and P_{bat} represents the total power delivered to the battery, that is, $P_{bat} = P_{pc} + P_{dir}$. The voltage withstood by the converter is denoted as V_{pc} , while the input and output voltage of the DC–DC regulation stage are represented by V_{in} and V_o , respectively. The voltage V_{pc} of Type I converters is determined by subtracting the input voltage V_i from the output voltage V_o . Type I PPCs connect the voltage V_{pc} in series with the output, making it more suitable for voltage step-up applications (resulting in a positive V_{pc}), since it only requires a unidirectional converter. On the other hand, Type II PPCs localize the voltage V_{pc} at the input, leading to a change in V_{pc} polarity. In this case, these converters are better for step-down processing with a unidirectional converter. Please note that, it is also possible to implement step-down Type I or step-up Type II PPCs; however, the need for bidirectional converters diminishes their appeal for such applications. In order to evaluate the level of partiality of Type I and Type II converters, a partial power ratio K_{ppr} is defined [18]. This ratio quantifies the amount of power that is processed directly by the converter in relation to its voltage gain G_v (further details of this ratio are provided later in Section 2.3). A comparison of the partial power ratio variation is presented in Figure 3. Assuming a voltage gain G_v within the range 0–2 both types of PPC are compared, since this is the typical gain of converters used in EV charging applications for either 400 and 800-V architectures. Please note that in both cases an input of 450 V is employed. Figure 3 illustrates that for 400-V systems, such as those employed in Tesla models, the voltage converters must perform a reduction of the voltage. For step-down operations, Type II converters are favoured because they can function as partial converters over a wider range, and the amount of power they manage is less than that of Type I converters. However, for 800-V architectures found in newer models such as the Porsche Taycan or Lucid Air models, step-up operation is required from the same input. Hence, for this mode of operation, a better performance of Type I convert-

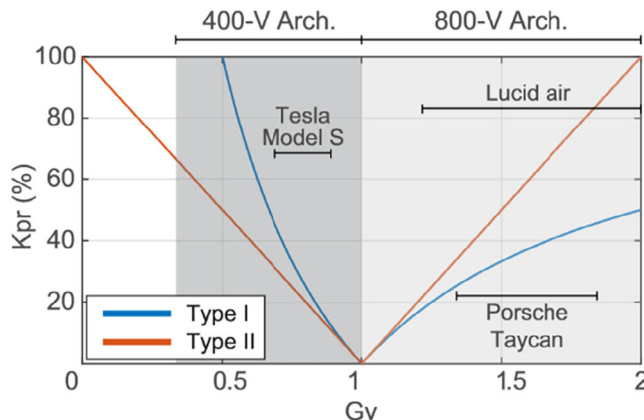


FIGURE 3 Partial power ratio converter of Type I and Type II PPC.

ers is clearly shown, since for a step-up operation they require to process than Type II converters. Then, if the converter operating in boost mode, the advantages of Type I over Type II converters can be explained as follows. As displayed in Figure 3, Type II converters gradually increase the power they handle to the point of no longer operating as PPC. In contrast, Type I PPCs do not face operating limits, because they keep operating in partial power mode despite increasing the converter gain. Furthermore, Type I PPCs in boost mode process a lower fraction of the power delivered to the battery compared to Type II PPCs [19, 25].

However, conventional PPC configurations are characterized by including a HF transformer in their topology [21, 25]. However, the HF transformer does not provide galvanic isolation to the system since the PPCs have a bypass connection between the primary and secondary of the transformer. This connection allows part of the power to pass directly without being handled by the converter, but disables the isolation, hence the autotransformer nature of such PPCs. In order to meet the isolation requirements, a low-frequency transformer is usually used as in Figure 1a, or alternatively the PPC can be used as a post-regulator DC–DC converter as in Figure 1c. The transformer is there to provide a functional task, which is to inject a series voltage at the output ($V_o = V_{in} + V_{pc}$ for Type I PPC), or at the input ($V_{in} = V_o + V_{pc}$ for Type II PPC). The transformer does

provide an extra degree of freedom in terms of turn-ratio design ($n_1:n_2$) that along with the phase-shift operation of the converter can give more flexibility to the input/output voltage gain. However, it comes at expense of extra losses, size and cost, without benefits of galvanic isolation. According to [26–28], by comparing isolated and non-isolated DC-DC converters that feature the same number of semiconductors, transformerless options can lead to a cost reduction between 51% and 57%.

In this article, a new transformerless step-up Type I PPC topology for 800 V battery chargers is presented. The HF transformer is replaced by an impedance network. This change makes the proposed converter lose the extra degree of freedom by not being able to design the turns ratio of the transformer. However, the phase shift of the converter generates a duty cycle through a phase-shift modulation (PSM), which is sufficient to regulate the battery charging process. Furthermore, the elimination of the transformer increases efficiency and power density, while reducing cost. The contribution also includes the switching states analysis, non-linear dynamic model of the converter, the transfer function derivation, efficiency analysis, partial power analysis, and the modulation and control of the system. Simulation and experimental tests are presented to validate the operation principle of the converter as a DC-DC regulation stage of an EV fast charging station.

The remainder of this article is structured as follows. Section 2 introduces the proposed converter, describing its topology, the principle of operation and the control scheme. Section 3 shows the simulation results and an efficiency analysis of the converter. Section 4 provides the experimental validation obtained in a laboratory prototype. Finally, Section 5 summarizes the conclusions of this work.

2 | PROPOSED PPC CONVERTER

2.1 | Topology description

This work proposes a new transformerless Type I DC-DC PPC designed to operate as the regulation DC-DC converter of a battery fast charging station. A conventional Type I PPC is presented in Figure 4a. It uses a full bridge connected via a HF transformer to the output rectifier bridge [29, 30]. Note that this HF transformer does not provide galvanic isolation because there is an electrical connection between the primary and secondary windings. This motivates the proposed converter shown in Figure 4b, where the transformer has been replaced by an impedance network, this network is composed of an arrangement of two capacitors and an inductor in order to avoid the HF transformer losses, extra size and cost. Considering Figure 2a, it can be seen that the proposed converter configuration corresponds to a series-connected Type I PPC. The input voltage V_{in} is connected in series to the partial voltage V_{pc} on the output of the secondary side of the converter.

The proposed converter considers the full-bridge configuration at the input and a diode-bridge in series to the output, producing a series voltage between the input DC-link and the battery. Depending on the switching state of the semiconduc-

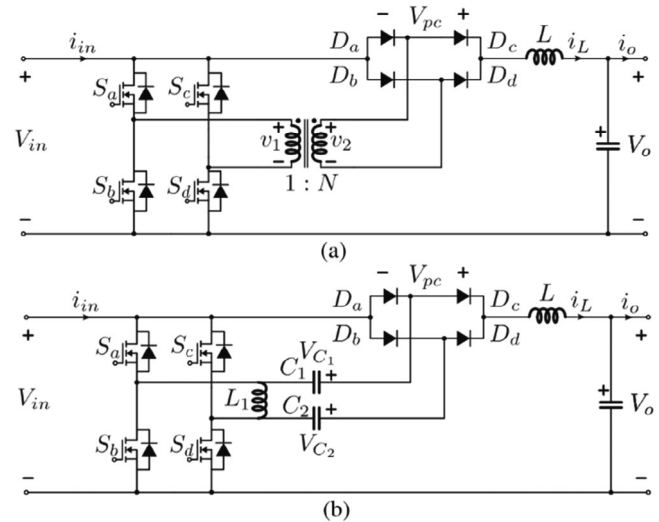


FIGURE 4 Step-up PPC Type I topologies. (a) Full-bridge topology with transformer. (b) Proposed transformerless full-bridge.

tors, the voltage across capacitors C_1 or C_2 is connected in series with the input voltage and the inductive output filter L . PSM has been employed to generate the switching states. This technique introduces a phase shift α between the voltages generated by the legs of the full-bridge in order to regulate the voltage rectified by the output diode bridge. This phase shift varies within the range 0–0.5 corresponding to a displacement from 0° to 180° . Depending on the output requirements, the switching signals of S_a and S_c are phase shifted accordingly. Then, since signals S_b and S_d are the binary complement of S_a and S_c respectively, exhibit the same phase delay.

The two topologies in Figure 4 use the output inductor L to control both the output voltage and current, allowing the converter to perform the charging process according to the charging profile imposed by the battery management system (BMS).

The steady-state waveforms of the converter are shown in Figure 5a,b show the gating signals of semiconductors S_a and S_c . Additionally the theoretical waveforms of the most important components of the proposed converter are displayed throughout a switching cycle. Figure 5c presents the drain to source voltage of the switch S_a over the course of an operation cycle. Then, Figure 5d,e shows the voltages in the capacitors of the impedance network. Please note that in steady state these capacitors are charged to a voltage level equal to the input, as it will be explained in Section 2.2. The behaviour of these components in a switching cycle is demonstrated. In state I, the capacitor C_1 is connected in series with the input, which in turn results in a fraction of the input current circulating in the direction of its voltage as displayed in Figure 5, hence leading to its discharge. On the other hand, the capacitor C_2 is connected in parallel with the input voltage, and its voltage increases in this state. Next, during state II, both capacitors are connected in parallel, and this arrangement is also connected in series with the input. Since the input current is divided through these capacitors, during this state both capacitors reduce their voltages. Later on,

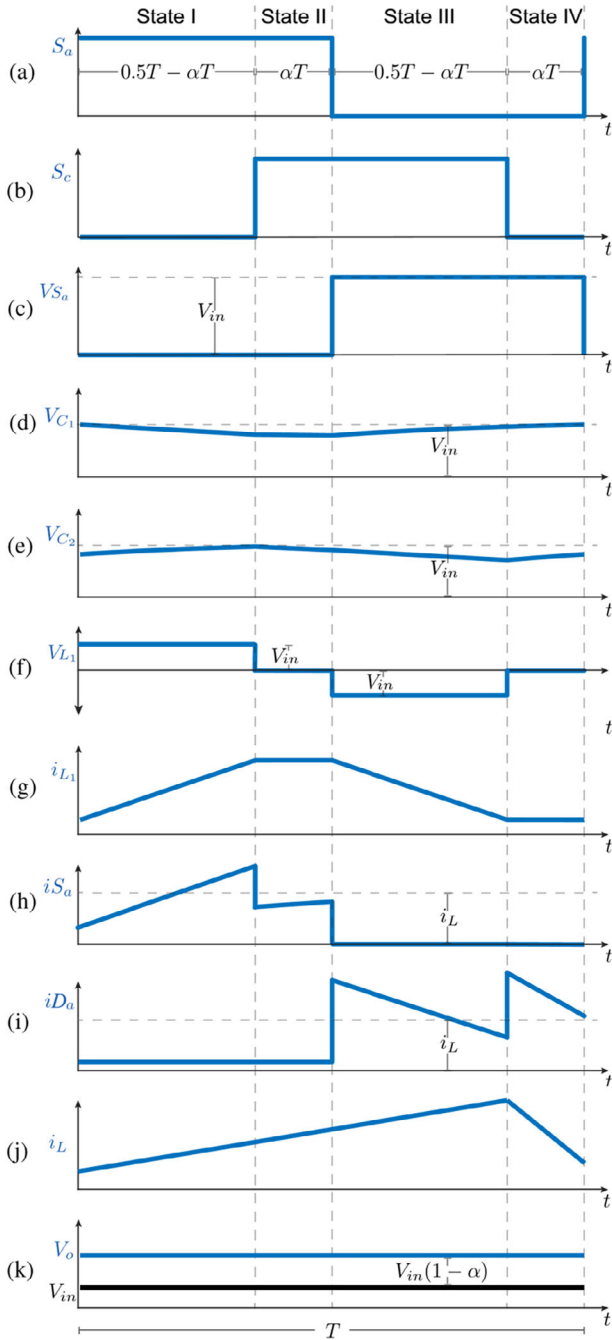


FIGURE 5 Steady-state operation waveforms. (a) S_a switching signal. (b) S_c switching signal. (c) S_a switching voltage. (d) C_1 capacitor voltage. (e) C_2 capacitor voltage. (f) L_1 inductor voltage. (g) L_1 inductor current. (h) S_a MOSFET current. (i) D_a diode current. (j) Output converter current. (k) Input and output converter voltages.

when state III is generated, the capacitor C_1 is charged while the capacitor C_2 is discharged, which is the opposite operation of the aforementioned state I. Finally, state IV connects the input source and both capacitors in parallel, resulting in both increasing their voltage. Conversely, Figure 5f,g shows the voltage and current in the impedance network inductor L_1 respectively. It is observed that for state I, the voltage applied is the same as the input voltage V_{in} , making its current to increase during this

interval. Then, the generation of states II and IV result in a zero-voltage applied to L_1 and thus its current will be kept constant. Then, during state III, the voltage applied is the negative of the input voltage V_{in} , making its current to decrease accordingly. Following that, Figure 5h displays the current flowing through the MOSFET S_a . It can be seen that it is conducting in both states in which its gate signal is on. MOSFETs must be able to handle a current that is larger than the output current of the converter, which is determined by the alpha displacement factor. Please note that the other MOSFETs drive a similar current with the corresponding phase shift according to the operation of a voltage-fed full bridge. Now, the current driven by the diodes of the system is represented in Figure 5i, which displays the current through the diode D_a . The operation of the converter will lead to the output current converter measured at the output inductor L , presented in Figure 5j. An important detail to consider is that, despite the similarity with conventional PPCs, the output signals do not have twice the switching frequency. Finally, Figure 5k shows the input voltage and output voltage of the converter, where the boost property of the converter can be observed.

2.2 | Operation principle

The proposed converter has four switching states obtained by the switching signals in the active bridge, as shown in Figure 6. In state I, corresponding to Figure 6a, the capacitor C_1 is connected in series with the input voltage and the voltage in the inductor L to the output. For switching state II shown in Figure 6b, the two capacitors C_1 and C_2 are connected in parallel and, at the same time, this arrangement is connected in series with the input voltage and output inductor voltage to the output. In state III, capacitor C_2 is connected in series with the input voltage and the voltage in the inductor L to and the output, as displayed in Figure 6c. Finally, in state IV depicted in Figure 6d, the capacitors of the impedance network are connected in parallel with the input of the converter, making the voltage V_{pc} equal to zero. Note that the switching states connecting the capacitors of the impedance network in series with the input voltage of the converter define the step-up nature of the converter.

The state variables equations can be obtained for each switching state and equivalent circuit of the converter, according to Figures 5 and 6. Considering T as the switching period, yields:

2.2.1 | Switching state I: $(S_a, S_c) = (1, 0)$, state duration $(0.5 - \alpha)T$

$$\begin{aligned}
 L_1 \frac{di_1}{dt} &= V_{in} \\
 V_{c_2} &= V_{in} \\
 C_1 \frac{dV_{c_1}}{dt} &= -i_L \\
 L \frac{di_L}{dt} &= V_{in} + V_{c_1} - V_o \\
 C_o \frac{dV_o}{dt} &= -i_L - i_o
 \end{aligned} \tag{1}$$

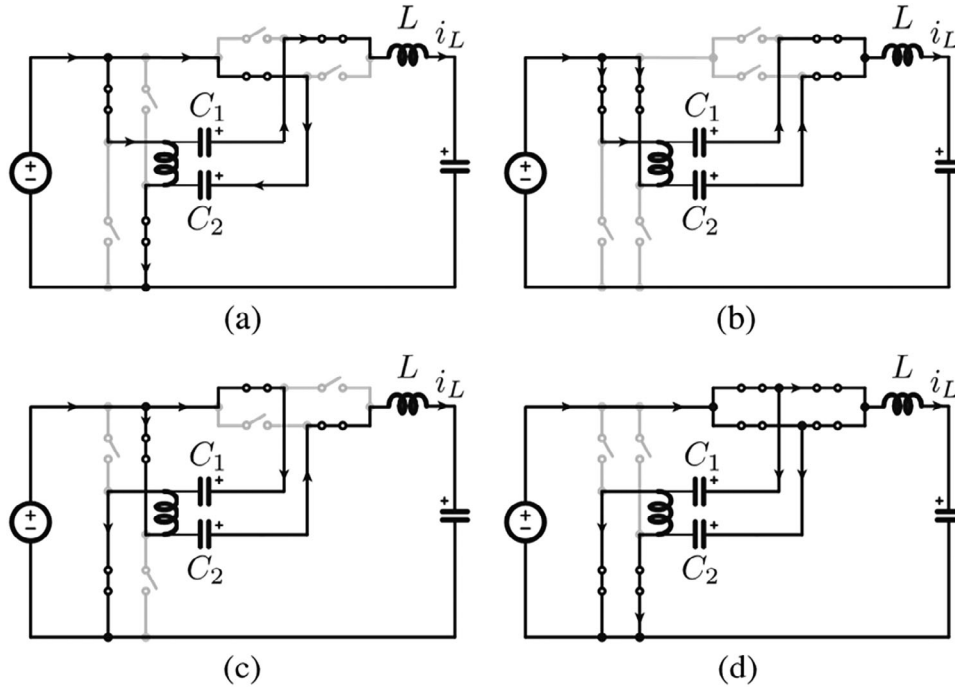


FIGURE 6 Switching states of the converter. (a) State I $(S_a, S_c) = (1, 0)$. (b) State II $(S_a, S_c) = (1, 1)$. (c) State III $(S_a, S_c) = (0, 1)$. (d) State IV $(S_a, S_c) = (0, 0)$.

2.2.2 | Switching state II: $(S_a, S_c) = (1, 1)$, state duration αT

$$\begin{aligned}
 L_1 \frac{di_1}{dt} &= 0 \\
 V_{c_1} &= V_{c_2} \\
 C_1 \frac{dV_{c_1}}{dt} + C_2 \frac{dV_{c_2}}{dt} &= -i_L \\
 L \frac{di_L}{dt} &= V_{in} + V_{c_1} - V_o \\
 C_o \frac{dV_o}{dt} &= i_L - i_o
 \end{aligned} \quad (2)$$

2.2.3 | Switching state III: $(S_a, S_c) = (0, 1)$, state duration $(0.5 - \alpha)T$

$$\begin{aligned}
 L_1 \frac{di_1}{dt} &= -V_{in} \\
 V_{c_1} &= V_{in} \\
 C_2 \frac{dV_{c_2}}{dt} &= -i_L \\
 L \frac{di_L}{dt} &= V_{in} + V_{c_2} - V_o \\
 C_o \frac{dV_o}{dt} &= i_L - i_o
 \end{aligned} \quad (3)$$

2.2.4 | Switching state IV: $(S_a, S_c) = (0, 0)$, state duration αT

$$\begin{aligned}
 L_1 \frac{di_1}{dt} &= 0 \\
 V_{c_1} &= V_{in} \\
 V_{c_2} &= V_{in} \\
 L \frac{di_L}{dt} &= V_{in} - V_o \\
 C_o \frac{dV_o}{dt} &= i_L - i_o
 \end{aligned} \quad (4)$$

The state-space representation of the system turns out to be non-linear and discontinuous, making its analysis complex. In order to simplify the analysis of the system, state-space averaging is used. This basic approximation allows removing the HF switching ripple by averaging over one switching period. For this purpose, a reduced-order dynamic average model is considered. The average value is calculated over a switching period, according to:

$$\bar{x} = \frac{1}{T} \int_t^{t+T} x(\tau) \cdot d\tau \quad (5)$$

where $\bar{x}(t)$ is the average of $x(t)$ over a switching period T . According to the state-space equations from (1) to (4), the state-space large-signal average equation for the output inductor can

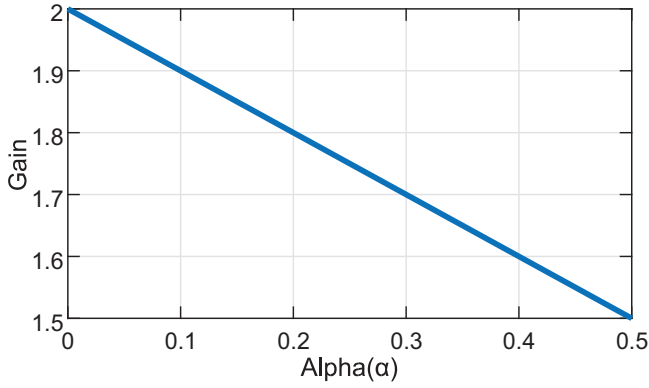


FIGURE 7 Gain of the proposed converter as a function of the phase shift α .

be derived as:

$$\begin{aligned} L \frac{d\bar{i}_L}{dt} &= (0.5 - \alpha) (\bar{V}_o - \bar{V}_{C1} - V_{in}) \\ &+ \alpha (\bar{V}_o - \bar{V}_{C1} - V_{in}) + (0.5 - \alpha) (\bar{V}_o - \bar{V}_{C2} - V_{in}) \\ &+ \alpha (\bar{V}_o - \bar{V}_{C1}) \end{aligned} \quad (6)$$

The output capacitor state-space average equation is:

$$C_o \frac{d\bar{V}_o}{dt} = \bar{i}_L - \bar{i}_o \quad (7)$$

For simplification purposes, the following hypothesis is considered:

$$\bar{V}_{C1} = \bar{V}_{C2} = V_{in}. \quad (8)$$

Rewriting (6) results in:

$$L \frac{d\bar{i}_L}{dt} = (\alpha) (\bar{V}_o - V_{in}) + (\bar{V}_o - 2V_{in}) (1 - \alpha) \quad (9)$$

Considering the system in steady-state operation, that is, $\frac{d\bar{i}_L}{dt} = 0$, the input-to-output transfer function of the system is obtained, as follows:

$$\frac{\bar{V}_o}{V_{in}} = 2 - \alpha \quad (10)$$

From (10) it is clear that the converter is capable of boosting the voltage between a factor of 1.5 and 2 depending on the phase shift α . The converter gain as a function of the phase shift α is shown in Figure 7.

2.3 | Partial power converter analysis

In order to analyze the partiality of the proposed converter, the partial power ratio K_{pr} , can be defined as the ratio

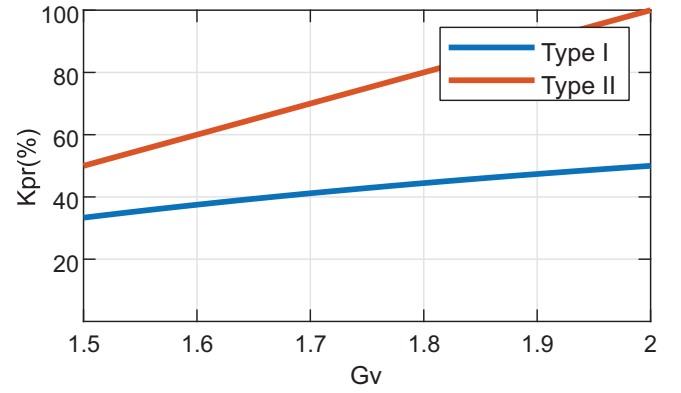


FIGURE 8 Partial power operation range for Type I and Type II partial power converters.

between the power handled by the PPC in relation to the input power of the whole DC–DC stage:

$$K_{pr} = \frac{|P_{pc}|}{P_{in}} \quad (11)$$

In addition, the converter voltage gain G_v can be defined as the ratio between the output and input voltage:

$$G_v = \frac{V_o}{V_{in}} \quad (12)$$

For a Type I PPC, considering ideal components, the partial power ratio is given by [18, 21]:

$$K_{pr} = 1 - \frac{1}{G_v} \quad (13)$$

On the other hand, the ideal partial power ratio for a Type II PPC is given by [18, 21]:

$$K_{pr} = G_v - 1 \quad (14)$$

The partial power ratio K_{pr} varies depending on the voltage gain G_v of the converter, as shown in Figure 8. This value shows the proportion of power handled by the converter; the remaining fraction is directly supplied to the battery. Figure 8 shows the particular case for the converter proposed in this article; the maximum gain value of the converter corresponds to $G_v = 2$, a value for which the partial power ratio reaches 50%, for Type I PPC, for the minimum gain value of the converter, $G_v = 1.5$ the partial power ratio reaches 33%. Hence, the proposed converter is capable of feeding the load with full power, while processing only a fraction of it. Several PPC applications have operating points at which the level of the bias ratio is in similar ranges [21, 31–33]. Figure 8 also shows the behaviour of a Type II PPC in the same operating range. It can be seen that within the entire operating range the partial power ratio for a Type II PPC is higher than for a Type I PPC, that is, the power that the Type II

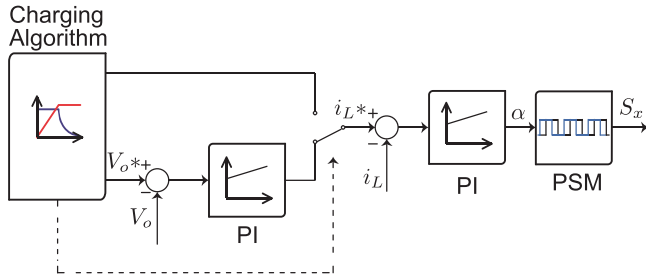


FIGURE 9 Constant current/constant voltage control scheme.

converter will handle is higher, so choosing a Type I converter is better suited for this application.

2.4 | Control scheme

A conventional cascaded control scheme is used to regulate the charging process of the battery, as shown in Figure 9. The external PI controller is responsible for regulating the output voltage of the converter, while the internal PI controller is used to regulate the output current. The cascade control scheme can be bypassed to a single output current control loop to implement the constant current/constant voltage (CC–CV) charging algorithm [34]. During the first stage of the charging process, the reference for the internal current controller is set to a constant value indicated by the BMS, so that the charging station can operate at battery nominal current, hence no external voltage control loop is needed and is therefore bypassed. As soon as the battery voltage reaches a value predetermined by the BMS (usually a value associated with a range between 80% and 90% of the state-of-charge of the battery), the current reference changes, from the constant value to the output of the voltage controller, for which the outer control loop is engaged. During this stage of the charging process, the battery itself determines how much current is required to complete the charge without incurring in damaging over-voltages.

Regardless of the operating mode, the output of the current controller corresponds to the phase shift α , the same one that, through a PSM, generates the gating signals for the semiconductors of the proposed converter. The transfer functions used to design the PI controllers are obtained through a linearization of the non-linear model given by (10) and (11). This analysis is presented in Appendix A.

3 | SIMULATION RESULTS

3.1 | Charging process

To further analyze the proposed configuration, a simulation has been implemented using PLECS software. The battery has been modelled using an RC Li-ion model [35]. The parameters of the components used in the simulation are shown in Table 1.

TABLE 1 Simulation parameters.

Parameter	Value
Converter nominal power	160 kW
Input voltage	400 V
Nominal output current	200 A
Output inductor L	180 μ H
Impedance network inductor L_1	250 μ H
Impedance network capacitors $C_{1,2}$	200 μ F
Switching frequency	20 kHz
Battery capacity	60 kWh

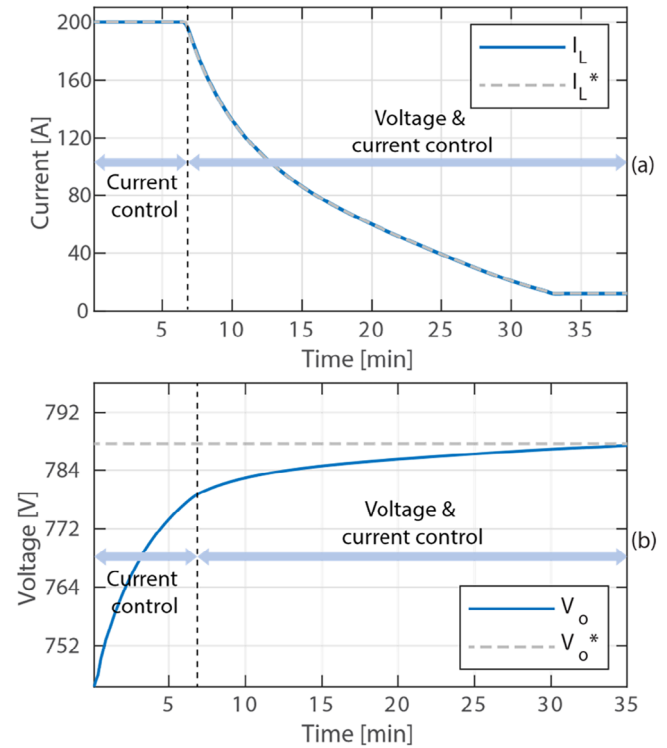


FIGURE 10 Battery charging process with the proposed converter. (a) Battery current. (b) Battery voltage.

A simulation over a whole battery charging cycle is shown in Figure 10. It can be seen that the behaviour of the converter follows the CC–CV charging algorithm. Figure 10a shows the current injected into the battery during the first five minutes when the charging station is in CC mode. When the battery reaches 80% of its state-of-charge, the BMS changes the current reference so that it is now set by the voltage controller. It can be seen that the CC follows the nominal current of the charger until around 6.5 min, the instant in which the current injected into the battery begins to reduce gradually. The charging process continues in a controlled manner until the battery reaches its maximum charge value indicated by the voltage reference of the external CV controller, as shown in Figure 10b.

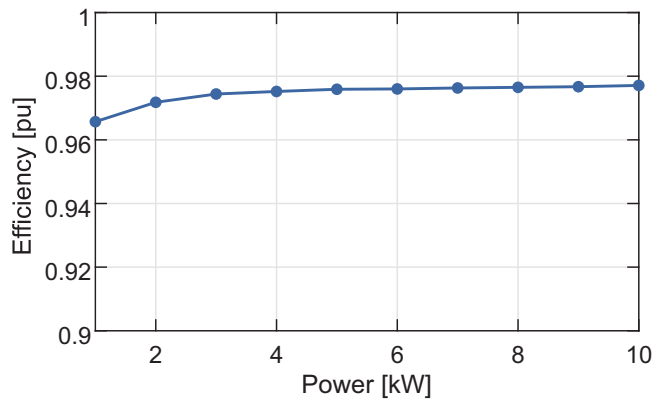


FIGURE 11 Simulated efficiency of proposed converter.

3.2 | Efficiency analysis

To carry out the efficiency analysis of the converter, the thermal modelling tool of PLECS was used for the C3M0025065D MOSFET and the GD2X20MPS12D diode. Usually, fast charging stations, in order to achieve a higher power rating, implement the DC–DC converter as an interleaved connection of several modules rated somewhere between 10 and 30 kW. In this simulation a 10 kW rated converter modules has been considered for the efficiency analysis. The study was carried out considering an operating power range between 1 and 10 kW for a 800 V nominal output voltage battery, obtaining the results shown in Figure 11. As with other DC–DC converters, the proposed topology can be implemented in an interleaved connection mode across multiple modules to reach higher power levels. This approach not only enhances power quality and reduces inductor sizes but also facilitates scalability to achieve battery chargers with higher power ratings. The interleaved connection can also further increase efficiency.

The estimated efficiency of the proposed converter is quite flat over the tested power range, particularly from half to rated power, and goes from a minimum 97% achieved at low capacity to a peak efficiency of 97.7% when operating at the highest power level. The efficiency of the converter is determined when it is running with a gain of $G_p = 2$, as discussed in earlier sections. This gain results in the converter operating at a 50% of partiality. The flat efficiency curve of the proposed converter makes it very attractive, since usually only high peak efficiencies are achieved for a narrow operating range in conventional charging stations. This can have an important impact over the global efficiency over the whole charging process, since usually peak efficiencies are only achieved through brief periods of time.

4 | EXPERIMENTAL RESULTS

A reduced-scale laboratory prototype based on silicon carbide (SiC) MOSFETs has been built to validate the proposed converter. Figure 12 shows the laboratory prototype. For the active H-bridge, the SiC G3R40MT12D MOSFET was used, while for the passive rectifier that is connected to the output

TABLE 2 Experimental parameters.

Parameter	Value
Input voltage V_{in}	150 V
Output voltage V_o	300 V
Output current I	4 A
Output current II (charger mode)	3 A
Output inductor L	1 mH
Impedance network inductor L_1	0.625 mH
Impedance network capacitors C_1	10 μ F
Impedance network capacitors C_2	10 μ F
Switching frequency f_{sw}	10 kHz
Battery capacity	10 Wh
MOSFETs	C3M0025065D
Diodes	GD2X20MPS12D

inductor, the GD2X20MPS12D diodes were used. The dead time of the H-bridge circuit was considered in the hardware when designing the control boards for the semiconductor gating signals. The parameters used for the experimental results are listed in Table 2.

As input of the converter, emulating the DC-link that is generated by the AC–DC rectifier of the charging station, the Chroma 62020H-150S programmable supply has been used. To emulate the EV battery a Chroma 62060-D bidirectional power supply has been used as load connected to the output terminals of the proposed converter. It has been configured to the battery voltage, capacity, and initial state-of-charge. The control of the converter is implemented using the dSpace MicroLabBox platform.

Figure 13 shows the validation of the transfer function of the system derived in (10), compared to the same curve obtained experimentally. A maximum error of 2% has been achieved between the experimental and theoretical results throughout the range of the phase shift α , validating the analytical derivation of the model of the converter.

The main waveforms of the converter are preliminary validated using a purely resistive load ($R = 100 \Omega$) connected to the output terminals. This test was carried out in open-loop, and no phase shift is imposed between the primary bridge legs ($\alpha = 0$). This results in an output voltage equal to the double the input voltage. This can be appreciated in Figure 14a where results for an input voltage value of 150 V are shown, including: channel 1 (yellow) corresponds to the output voltage of the converter at twice the input voltage (300 V); Channel 2 (green) shows the C_1 capacitor voltage, and it can be seen that this voltage is always equal to the input voltage; Channels 3 (blue) and 4 (red) display the input and output current measurements respectively. Since it is a boost converter, the output current is lower than the input current. For this case, the value of the output current of 3 A is determined by the resistive load used for the test.

Channel 1 (yellow) of Figure 14b shows the output voltage of the converter again, while channel 3 (blue) shows the voltage across switch S_b ; the maximum voltage that the semiconductors

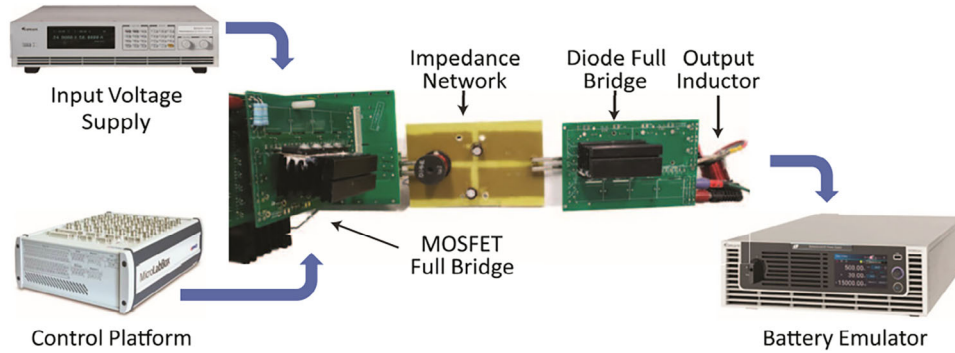


FIGURE 12 Experimental setup.

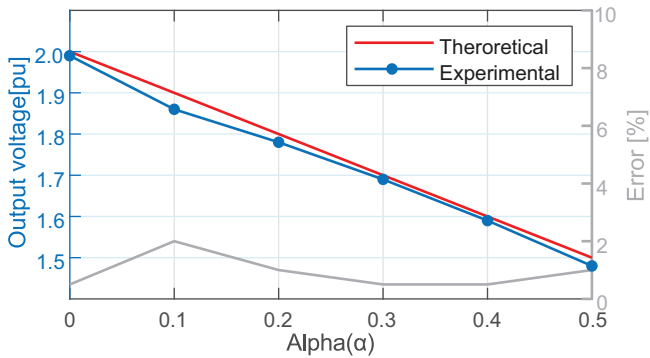


FIGURE 13 Transfer function experimental validation.

withstand during switching, unlike a traditional boost converter, is equal to the input voltage (it switches between 0 and 150 V). This feature allows sizing the MOSFETs with nominal values lower than the output voltage. Finally, channel 2 (green) shows the impedance network inductor voltage V_{L1} , switching between -150 and 150 V as expected.

In addition, a closed-loop battery charging process was tested, using the Chroma 62060-D bidirectional power supply to emulate the battery. The control profile is programmed in the local CPU and interfaced with the converter through a dSpace MicroLabBox. The results of the test are displayed in Figure 15, which provides a visual representation of the current and voltage profiles in steady-state operation. In order to speed up an entire charge cycle, the battery is simulated with a reduced capacity, as shown in Table 2.

The battery emulator used in this test was programmed to operate at 300 V with an initial state-of-charge of 60%. This produced an initial voltage of 264 V. The behaviour of the converter during steady-state was captured in a reduced timescale. Channel 1 (yellow) shows the battery voltage, charged with constant current of 3 A, which is shown in channel 4 (red). Channel 2 (green) shows the voltage in capacitor C_1 ; regardless of the state-of-charge of the battery voltage, the capacitor voltage always equals the input voltage, keeping its value at 150 V. Channel 3 (blue) shows the voltage across switch S_b . In the same way, as for the test carried out with resistive load, the voltage in the semiconductors varies between 0 and 150 V.

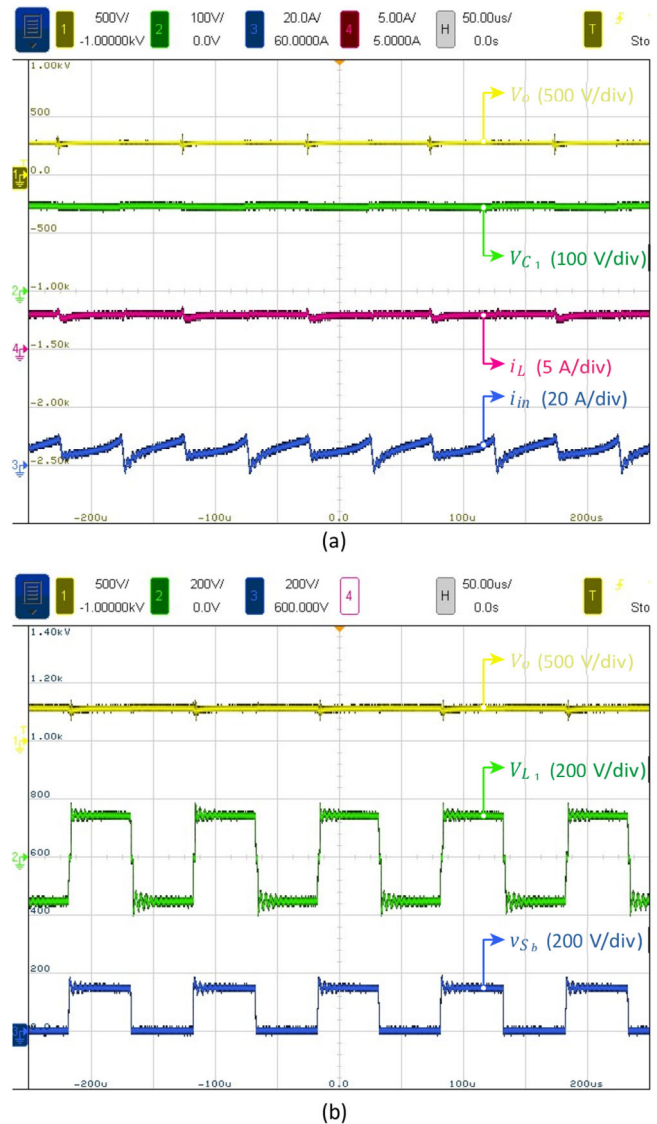


FIGURE 14 Experimental results with resistive load and $\alpha = 0.5$. (a) Ch1: Output voltage V_o , Ch2: Capacitor voltage V_{C1} , Ch3: Output current i_L , Ch4: Input current i_{in} . (b) Ch1: Output voltage V_o , Ch2: Impedance network inductor voltage V_{L1} , Ch3: switch S_b drain-source voltage.

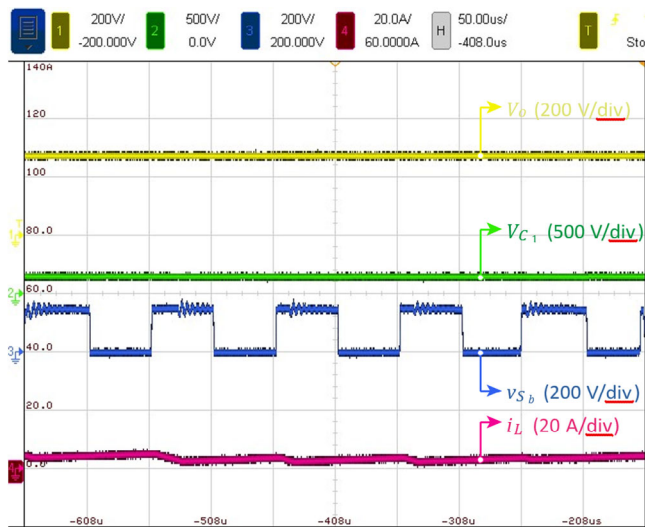


FIGURE 15 Experimental results during battery charging cycle. Ch1: Output voltage V_o , Ch2: Impedance network capacitor voltage V_{C1} , Ch3: switch S_b voltage, Ch4: Output current i_L .

4.1 | Experimental efficiency analysis

An experimental efficiency examination of the converter was conducted using the Yokogawa Precision Power Analyzer WTE3000E with the same parameters of the components listed in Table 2.

The results obtained in the efficiency analysis are shown in Figure 16, as well as a screenshot that indicates the measured input and output active powers, voltages, currents, and global efficiency of the proposed PPC. The power range that was studied exhibits the same features as the efficiency curve that was obtained from the simulation. The prototype constructed with a modular characteristic achieved a maximum efficiency of 95.35%, the modular characteristic with which the experimental prototype was built influences the slight difference between the results of Figures 11 and 16.

5 | CONCLUSION

Here, a new step-up transformerless PPC Type I topology is presented to be used as DC–DC regulation converter for EV fast charging stations, aimed at 800-V battery powertrains. The operating principle and mathematical model of the converter have been derived and validated through simulation and experimental results.

The topology has been derived from a typical PPC Type I, by replacing the HF transformer by an impedance network capable of connecting voltages in series to the input voltage to boost the output voltage with a nominal gain of 2.

The advantage of the proposed converter over traditional boost converters lies in the fact that the voltage blocked by the semiconductors and the passive components of the circuit is equal to the input voltage, which allows them to be sized with lower nominal values, making this a cost-effective solution.

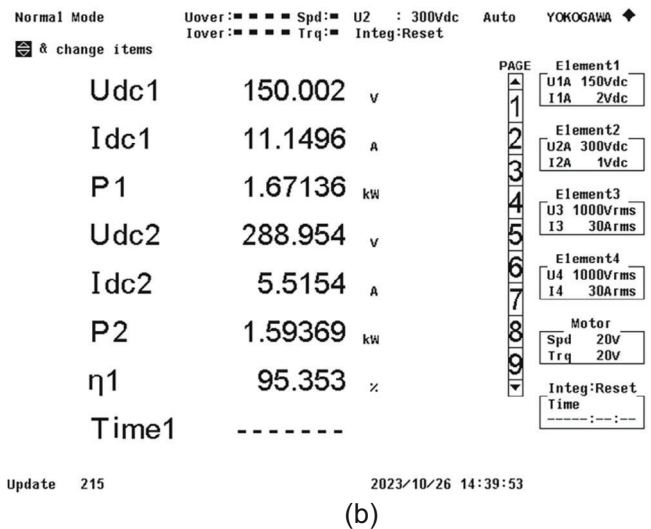
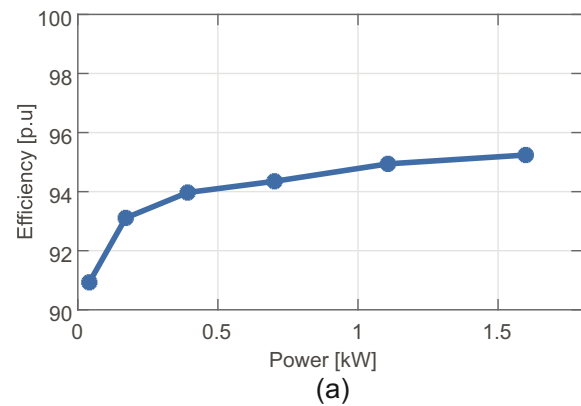


FIGURE 16 Experimental efficiency measurement of the proposed converter. (b) Measured input and output powers, voltages, currents, and global efficiency of the proposed PPC.

The validity of the proposed converter was verified through simulation and experimental results. The experimental comparison with the model showed a maximum error of 2%. In a simulation analysis, it was possible to estimate the efficiency of the converter operating within a range typical for a charging station power module. The peak efficiency achieved of 97.7% for nominal power of 10 kW is practically flat all over the operating range, enabling a high efficiency charging process, and an experimental efficiency analysis, with a peak laboratory efficiency of 95.35%.

The operating principle, waveforms, and converter gain were experimentally validated through a reduced-scale laboratory prototype, including an emulated battery charging process.

The proposed converter is an attractive transformerless PPC alternative for the DC–DC regulation stage for EV fast charging stations.

AUTHOR CONTRIBUTIONS

Hugues Renaudineau: Conceptualization; formal analysis; investigation; methodology; supervision; validation; writing—review and editing. **Sebastian Rivera:** Formal analysis; investigation; methodology; supervision; validation; writing—review

and editing. **Alejandro Peralta**: Data curation; methodology; resources; software. **Abraham Marquez Alcaide**: Supervision; validation; visualization; writing—review and editing. **Samir Kouro**: Conceptualization; funding acquisition; investigation; project administration; supervision; validation; visualization; writing—review and editing.

ACKNOWLEDGEMENTS

The authors gratefully acknowledge the financial support by ANID-Fondecyt 1221741, AC3E (ANID/BASAL/FB0008), SERC (ANID/FONDAP/1522A0006), ANID/FONDEQUIP/EQM180215, ANID-Subdirección de Capital Humano/ Doctorado Nacional/2022/21221405, Dirección de Postgrado y Programas Universidad Técnica Federico Santa María.

CONFLICT OF INTEREST STATEMENT

The authors declare no conflicts of interest.

DATA AVAILABILITY STATEMENT

Data available on request from the authors

ORCID

Daniel Pesantez  <https://orcid.org/0009-0008-3363-0734>

Hugues Renaudineau  <https://orcid.org/0000-0002-3492-4979>

Sebastian Rivera  <https://orcid.org/0000-0002-7991-2234>

Alejandro Peralta  <https://orcid.org/0009-0007-0218-4164>

Abraham Marquez Alcaide  <https://orcid.org/0000-0003-1647-7527>

Samir Kouro  <https://orcid.org/0000-0002-1690-4624>

REFERENCES

- IEA: Global EV outlook 2023 <https://www.iea.org/reports/global-ev-outlook-2023> (2023). Accessed 15 May 2023
- Jung, C.: Power up with 800-V systems. *IEEE Electr. Mag.* 5(1), 53–58 (2017)
- Rivera, S., Kouro, S., Vazquez, S., Goetz, S.M., Lizana, R., Romero-Cadaval, E.: Electric vehicle charging infrastructure: from grid to battery. *IEEE Ind. Electron. Mag.* 15(2), 37–51 (2021)
- Rivera, S., Goetz, S.M., Kouro, S., Lehn, P.W., Pathmanathan, M., Bauer, P., Mastromauro, R.A.: Charging infrastructure and grid integration for electromobility. *Proc. IEEE* 111(4), 371–396 (2022)
- Wang, L., Qin, Z., Slangen, T., Bauer, P., van Wijk, T.: Grid impact of electric vehicle fast charging stations: Trends, standards, issues and mitigation measures an overview. *IEEE Open J. Power Electron.* 2, 56–74 (2021)
- Cano, Z.P., Banham, D., Ye, S., Hintennach, A., Lu, J., Fowler, M., Chen, Z.: Batteries and fuel cells for emerging electric vehicle markets. *Nat. Energy* 3(4), 279–289 (2018)
- Scott, M.: Ever-cheaper batteries bring cost of electric cars closer to gas guzzlers. <https://www.forbes.com/sites/mikescott/2020/12/18/ever-cheaper-batteries-bring-cost-of-electric-cars-closer-to-gas-guzzlers/?sh=7439281b73c1> (2020). Accessed 1 July 2023
- Srdic, S., Lukic, S.: Toward extreme fast charging: challenges and opportunities in directly connecting to medium-voltage line. *IEEE Electr. Mag.* 7(1), 22–31 (2019)
- Tu, H., Feng, H., Srdic, S., Lukic, S.: Extreme fast charging of electric vehicles: A technology overview. *IEEE Trans. Transp. Electr.* 5(4), 861–878 (2019)
- Singh, B., Kushwaha, R.: A pfc based ev battery charger using a bridgeless isolated sepic converter. *IEEE Trans. Ind. Appl.* 56(1), 477–487 (2020)
- Shi, R., Semsar, S., Lehn, P.W.: Constant current fast charging of electric vehicles via a dc grid using a dual-inverter drive. *IEEE Trans. Ind. Electron.* 64(9), 6940–6949 (2017)
- Oulad-Abbou, D., Doubabi, S., Rachid, A., Garcia-Trivino, P., Fernandez-Ramirez, L.M., Carlos, F.R., Garcia-Vazquez, A., Sarrias-Mena, R.: Combined control of MPPT, output voltage regulation and capacitors voltage balance for three-level DC/DC boost converter in PV- EV charging stations. In: *SPEEDAM 2018 - Proceedings: International Symposium on Power Electronics, Electrical Drives, Automation and Motion*. Amalfi, Italy, pp. 372–376 (2018)
- Safaeinasab, A., Gohari, H.S., Abbaszadeh, K.: Design and control of a novel multi-port bidirectional buck-boost converter suitable for hybrid electric vehicle charging stations. In: *2022 30th International Conference on Electrical Engineering, ICEE 2022*. Tehran, Iran, pp. 1027–1032 (2022)
- Ma, J., Deng, Y., Wen, S., Zhu, M.: Multimode operation of buck-boost converter for building block of DC fast charging station. In: *Conference Record—IAS Annual Meeting (IEEE Industry Applications Society)*, pp. 1–6. Detroit, MI, USA (2022)
- Soeiro, T., Friedli, T., Kolar, J.W.: Three-phase high power factor mains interface concepts for electric vehicle battery charging systems. In: *Conference Proceedings—IEEE Applied Power Electronics Conference and Exposition APEC*, pp. 2603–2610. Orlando, FL, USA (2012)
- Erickson, R.W., Maksimovic, D.: *Fundamentals of Power Electronics*, 2nd ed., pp. 501–524. Springer, Berlin (2012)
- Zanatta, N., Caldognetto, T., Biadene, D., Spiazzi, G., Mattavelli, P.: Analysis and design of a partial-power post-regulator-based dc/dc converter for automotive applications. In: *2022 IEEE 13th International Symposium on Power Electronics for Distributed Generation Systems (PEDG)*, pp. 1–6. Kiel, Germany (2022)
- Zapata, J.: Partial power DC–DC converters for two stage photovoltaic energy conversion systems. Ph.D. Dissertation, Universidad Tecnica Federico Santa Maria (2018)
- Anzola, J., Aizpuru, I., Romero, A.A., Loiti, A.A., Lopez-Erauskin, R., Artal-Sevil, J.S., Bernal, C.: Review of architectures based on partial power processing for DC–DC applications. *IEEE Access* 8, 103405–103418 (2020)
- Rivera, S., Pesantez, D., Kouro, S., Lehn, P.W.: Pseudo-partial-power converter without high frequency transformer for electric vehicle fast charging stations. In: *2018 IEEE Energy Conversion Congress and Exposition, ECCE 2018*, pp. 1208–1213. Portland, OR, USA (2018)
- Rivera, S., Rojas, J., Kouro, S., Lehn, P.W., Lizana, R., Renaudineau, H., Dragicevic, T.: Partial-power converter topology of type II for efficient electric vehicle fast charging. *IEEE J. Emerging Sel. Top. Power Electron.* 10(6), 7839–7848 (2022)
- Iyer, V.M., Gulur, S., Gohil, G., Bhattacharya, S.: An approach towards extreme fast charging station power delivery for electric vehicles with partial power processing. *IEEE Trans. Ind. Electron.* 67(10), 8076–8087 (2020)
- Anzola, J., Aizpuru, I., Arruti, A.: Non-isolated partial power converter for electric vehicle fast charging stations. In: *2020 IEEE 11th International Symposium on Power Electronics for Distributed Generation Systems, PEDG 2020*, pp. 18–22. Dubrovnik, Croatia (2020)
- Rivera, S., Flores-Bahamonde, F., Renaudineau, H., Dragicevic, T., Kouro, S.: A buck-boost series partial power converter using a three-port structure for electric vehicle charging stations. In: *2021 IEEE 12th Energy Conversion Congress and Exposition—Asia (ECCE-Asia)*, pp. 1749–1754. Singapore, Singapore (2021)
- Zientarski, J.R.R., Da Silva Martins, M.L., Pinheiro, J.R., Hey, H.L.: Series-connected partial-power converters applied to PV systems: A design approach based on step-up/down voltage regulation range. *IEEE Trans. Power Electron.* 33(9), 7622–7633 (2018)
- Agheb, E., Hoidalén, H.K.: Medium frequency high power transformers, state of art and challenges. In: *2012 International Conference on Renewable Energy Research and Applications (ICRERA)*, pp. 1–6. Nagasaki, Japan (2012)
- Barrios, E.L., Urtasun, A., Ursúa, A., Marroyo, L., Sanchis, P.: High-frequency power transformers with foil windings: Maximum interleaving

- and optimal design. *IEEE Trans. Power Electron.* 30(10), 5712–5723 (2015)
28. Zhou, L., Jahnes, M., Eull, M., Wang, W., Preindl, M.: Control design of a 99efficiency transformerless EV charger providing standardized grid services. *IEEE Trans. Power Electron.* 37(4), 4022–4038 (2022)
 29. Song, H., Xu, R., Gao, S., Wang, Y., Xu, D.: A high-frequency dual active bridge converter with partial power processing. In: PEAC 2022 - 2022 IEEE International Power Electronics and Application Conference and Exposition, Proceedings, pp. 258–263. Guangzhou, Guangdong, China (2022)
 30. Beckmann, C.S., Rojas, C.A., Renaudineau, H., Kouro, S., Young, H., Opazo, R., Rivera, S.: Comparison of modulation strategies for a dual active bridge partial power DC–DC converter in EV powertrains. In: IECON Proceedings (Industrial Electronics Conference), pp. 3–8. Brussels, Belgium (2022)
 31. Renaudineau, H., Pesantez, D., Muller, N., Flores-Bahamonde, F., Kouro, S., Rodriguez, J.: Reconfigurable step-up/down partial power converter for PV power optimizer. In: 2022 IEEE Energy Conversion Congress and Exposition (ECCE), pp. 1–6. Detroit, MI, USA (2022)
 32. Guo, B., Zhang, X., Zhang, Z., Ma, H., Jin, X., Wang, Y.: Design of a 300 kW partial power processing based dc-dc converter for electric vehicles extreme fast charging stations. In: 2022 IEEE International Power Electronics and Application Conference and Exposition (PEAC), pp. 423–428. Guangzhou, Guangdong, China (2022)
 33. Anzola, J., Artal-Sevil, J.S., Aizpuru, I., Arruti, A., Lopez, R., Alacano, A., Bernal-Ruiz, C.: Resonant dual active bridge partial power converter for electric vehicle fast charging stations. In: 2021 IEEE Vehicle Power and Propulsion Conference (VPPC), pp. 1–6. Gijon, Spain (2021)
 34. Shen, W., Vo, T.T., Kapoor, A.: Charging algorithms of lithium-ion batteries: An overview. In: 2012 7th IEEE Conference on Industrial Electronics and Applications (ICIEA), pp. 1567–1572. Singapore, Singapore (2012)
 35. Kou, S., Gong, X., Zhu, Q., Wang, G.: Parameter identification of battery model based on forgetting factor recursive least square method. In: Proceedings of 2018 IEEE 4th Information Technology and Mechatronics Engineering Conference, ITOEC, pp. 1712–1715. Chongqing, China (2018)

How to cite this article: Pesantez, D., Renaudineau, H., Rivera, S., Peralta, A., Marquez Alcaide, A., Kouro, S.: Transformerless partial power converter topology for electric vehicle fast charge. *IET Power Electron.* 1–13 (2023). <https://doi.org/10.1049/pel2.12613>

APPENDIX A

From (6) and (7) it is possible to develop a model that allows the design the converter controllers by linearizing them. A small-signal model around a quiescent operating point can be obtained through the perturb and observe technique. This approach was chosen due to its simplicity, which enabled the development of a mathematical model that accurately reflects the converter

[16]. Consequently, the design of controllers is made easier, and the system is made more resilient to noise or disturbances. It is worth noting that there are a variety of linearization techniques that are also effective for this purpose. A small disturbance $x^\wedge(t)$ is added to the input signals V_{in} and α , expecting that the other variables also present a small variation. Obtaining mainly the following equations:

$$\begin{aligned} \bar{V}_{in}(t) &= V_{in} + \hat{v}_{in}(t) \\ \alpha(t) &= A + \hat{\alpha}(t) \\ \bar{i}_L(t) &= I_{in} + \hat{i}_L(t) \\ \bar{V}_o(t) &= V_o + \hat{v}_o(t) \end{aligned} \quad (A.1)$$

Considering that the disturbances are very small compared to the signals, that is, $|\hat{v}_{in}(t)| \ll |V_{in}|$, $|\hat{\alpha}(t)| \ll |A|$, $|\hat{i}_L(t)| \ll |I_{in}|$ and $|\hat{v}_o(t)| \ll |V_o|$, equation (9) and (7) can be written as follows:

$$\begin{aligned} L \frac{d\hat{i}_L(t)}{dt} &= (A + \hat{\alpha}(t)) (V_o + \hat{v}_o(t) - (V_{in} + \hat{v}_{in}(t))) \\ &\quad + (A' + \hat{\alpha}(t)) (V_o + \hat{v}_o(t) - 2(V_{in} + \hat{v}_{in}(t))) \end{aligned} \quad (A.2)$$

$$C_o \frac{d\hat{V}_o(t)}{dt} = (I_L + \hat{i}_L(t)) - \frac{V_o + \hat{v}_o(t)}{R_{eq}} \quad (A.3)$$

where $A' = (1 - A)$, R_{eq} represents the equivalent output load.

Simplifying (A.2) and (A.3), three types of terms are distinguished. The first corresponds to multiplications of the constant terms, which equals zero around the quiescent operating point. The seconds correspond to the second-order terms, composed by multiplying the small disturbance signals among themselves; these being very small, can be neglected. These assumptions reduce the aforementioned equations to only their linear terms, resulting in the following:

$$L \frac{d\hat{i}_L(t)}{dt} = (\hat{\alpha})(V_{in}) + (A - 2)(V_{in}) + (V_o) \quad (A.4)$$

$$C_o \frac{d\hat{V}_o(t)}{dt} = \hat{i}_L(t) - \frac{\hat{v}_o(t)}{R_{eq}} \quad (A.5)$$

Solving equations (A.4) and (A.5) using Laplace transform, the resulting output-to-control transfer function is obtained:

$$\frac{V_o}{\alpha} = \frac{1.558s + 24.34}{0.7303s^2 + 23.1s - 38950} \cdot 10^5 \quad (A.6)$$